Article

Enhancement, brightening and control of radiative emission of dark exciton in WSe$_2$ monolayer by plasmonic effect

Check for updates

Adlen Smiri[1,2] ✉, F. R. Pratama[1,2] & Takeshi Nakanishi[1]

Dark excitons in two-dimensional (2D) transition metal dichalcogenide semiconductors (TMDs) have long radiative lifetimes, making them promising for quantum information and optoelectronics. Their detection and control are challenging due to weak out-of-plane dipole moments and momentum mismatch with free-space photons. Using ab initio calculations (DFT + G$_0$W$_0$ + BSE), a Wannier–Mott exciton model, and a numerical solution of the Laplace equation, we model the tip-enhanced near-field and its interaction with excitons via first-order time-dependent perturbation theory. Focusing on WSe$_2$ monolayers, we show that the strong out-of-plane near field from a metallic tip enhances radiative recombination of spin-forbidden dark excitons by providing additional in-plane momentum to overcome momentum mismatch. We also analyze substrate screening effects on excitonic properties and lifetimes. Our results offer a theoretical framework for controlled activation of dark excitons toward quantum and nanophotonic applications.

Excitonic states in two-dimensional (2D) transition metal dichalcogenide semiconductors (TMDs) exhibit diverse optical properties due to spin-orbit interactions and selection rules, making them central to emerging quantum optoelectronics. These materials follow the chemical formula MX$_2$, where M = W or Mo and X = S, Se, or Te[1,2]. Among the various excitonic states in 2D TMDs, dark excitons offer long radiative lifetime[3,4], making them attractive for applications such as quantum information processing[5] and Bose-Einstein condensation[6]. Understanding the mechanisms that activate these dark excitons is therefore crucial for unlocking their potential in quantum technologies.

Due to spin-orbit coupling (SOC), spin-splitting at the conduction and valence band extrema gives rise to various types of excitons[3,7]. Among them, two bright excitons, commonly known as A and B excitons, are characterized by spin and momentum conservation[1]. In contrast, dark excitons arise from transitions forbidden by momentum and/or spin conservation. These excitons are generally considered optically inactive under normal light excitation. They include spin-forbidden dark (SFD) excitons, which conserve momentum. In WX$_2$ (X = S, Se) monolayers, the SFD exciton lies below the bright exciton, making it the excitonic ground state[1,8,9]. In contrast, in MoX$_2$ (X = S, Se), the bright exciton is the lowest-energy excitonic state, and the SFD exciton lies at a higher energy[1,8,9]. The widely adopted terminology 'dark' for the SFD exciton is based on the fact that spin is not conserved during the transition. Therefore, efforts to brighten the SFD exciton have involved altering the spin direction and ensuring spin

conservation by applying a strong in-plane magnetic field[4,10]. However, different references[3,7,11,12] have shown that the SFD exciton is not dark even in the absence of a magnetic field.

According to group theory analysis, dipole selection rules permit SFD exciton transitions under z-polarized light[3,7,10]. Due to spin-orbit mixing, the spin of the bands involved in the SFD exciton is no longer a strict quantum number, allowing spin-forbidden transitions[3,7]. However, the out-of-plane dipole moment associated with the SFD exciton is predicted to be weak, approximately a hundred times smaller than that of the in-plane bright exciton dipole moment[7]. Consequently, the challenge lies in their weak out-of-plane transition dipole moments, which make these SFD excitons difficult to access optically.

To address this challenge, experiments have focused on enhancing the out-of-plane electric field to detect SFD excitons. One approach is surface plasmon polariton (SPP)-assisted near-field spectroscopy[12]. In this method, SFD excitons interact with surface plasmon polaritons, amplifying optical transitions with out-of-plane dipole moments. This enhancement enables their direct detection. Another approach uses high-numerical-aperture (high-NA) objectives to create focal tails that extend the electric field in the z-direction[7]. This generates a strong out-of-plane field, making SFD excitons optically accessible. These experiments were performed at low temperatures using WSe$_2$ monolayers, where SFD excitons dominate the emission due to their lower energy compared to bright excitons under cryogenic conditions[13].

[1]Mathematics for Advanced Materials Open Innovation Laboratory (MathAM-OIL), National Institue of Advanced Industrial Science and Technology, Sendai, Miyagi, Japan. [2]Advanced Institute for Materials Research, Tohoku University, Sendai, Miyagi, Japan. ✉e-mail: smiriadlen4@gmail.com

More recently, tip-enhanced photoluminescence (TEPL) spectroscopy (see Fig. 1) has enabled the observation of SFD excitons at room temperature[11]. TEPL further confines the electromagnetic field to the nanoscale, creating strong field enhancements near the tip apex. This allows for the selective excitation of SFD exciton states, offering superior spatial resolution and sensitivity in the study of quantum systems and 2D materials.

The brightening of SFD excitons has been experimentally attributed to the enhanced electric field along the z-axis, which compensates for the weak out-of-plane dipole moment[7,11,12]. However, the 2D exciton ground state, with zero in-plane dipole moment, remains dark due to unsatisfied momentum conservation[14]. To our knowledge, no theoretical framework fully explains the brightening of SFD excitons at the microscopic level, particularly in terms of both field enhancement and momentum mismatch. Our goal is to conduct an in-depth study to elucidate the mechanisms behind the activation of SFD excitons and to explore the potential to control their radiative lifetime in the presence of an Au tip.

Results

To investigate the tip effect on SFD exciton in WSe$_2$ ML, we first calculate the exciton properties of WSe$_2$ ML in the absence of the tip. We then compute the near-field enhancement around the metallic tip for a given incident light. Following this, we discuss the selection rules governing SFD exciton activation, comparing cases with and without the tip. Finally, we present the photoluminescence spectra and radiative lifetime of SFD excitons.

Excitonic properties of WSe$_2$ ML

Accurately modeling excitonic effects requires solving the Bethe–Salpeter Equation (BSE), which is derived from many-body perturbation theory[15,16]. The BSE allows the computation of excitonic properties, such as the dielectric function and exciton binding energies, without introducing additional parameters. However, solving the BSE is computationally demanding, particularly when including substrate effects. A practical alternative in such cases is the Wannier–Mott-exciton model in two-band approximation, which incorporates the screened Rytova-Keldysh potential[17,18] for electron-hole interactions. This approach has proven effective in determining exciton binding energies in previous studies[19–24].

The electronic bandstructure of WSe$_2$ ML is critical for determining its optical properties, as it governs the available electronic transitions that contribute to absorption, emission, and excitonic effects. To ensure accurate predictions of the optical properties of WSe$_2$ ML, the G_0W_0 correction was

used to obtain 2.03 eV, which aligns well with previous theoretical calculations[25]. To overcome the problem of the G_0W_0 indirect bandgap[25,26], we have considered a relaxation approach as presented in the supplement information. Our calculations reveal that interatomic distances, specifically the W-Se bond length and Se-W-Se bond angle, play a crucial role in determining the correct bandgap nature. As a result of this analysis, in Fig. 2a we show the electronic band structure of WSe$_2$ ML.

To investigate the excitonic properties relevant to emission in suspended WSe$_2$ MLs, we begin by computing the absorption spectrum using the Bethe–Salpeter equation (BSE). Although our primary interest lies in the emission (TEPL) characteristics, the BSE absorption spectrum provides crucial information on exciton energies and oscillator strengths, which also govern the radiative recombination rates. Given the high computational cost of G_0W_0 calculations, we use wave functions and energies obtained from the Perdew–Burke–Ernzerhof (PBE) calculations, applying a scissor operator derived from G_0W_0 for corrections. While this approach does not fully capture modifications in valence and conduction band dispersions, previous studies on MoS$_2$ ML (ref. 26) have shown that its impact on BSE calculations is negligible. This conclusion is further supported by the close agreement in effective masses presented in Supplementary Table 1 obtained from both G_0W_0 and PBE methods.

In Fig. 2b, we present the BSE absorption spectra of WSe$_2$ ML. The spectra are computed for two different light polarizations, activating distinct excitonic transitions as listed in Table 2. For in-plane polarization, we observe the characteristic absorption features of WSe$_2$ ML, where the low-energy peaks correspond to the A and B excitons. Additionally, a weak absorption peak appears at an energy slightly lower than the A exciton for out-of-plane (z-polarized) excitation. This peak corresponds to the SFD exciton, in agreement with dipole selection rules which will be discussed in details later.

Despite the accuracy of BSE in predicting excitonic properties, its high computational cost makes it impractical for the system in Fig. 1. Therefore, we employ the Wannier–Mott model, as detailed in the Microscopic Model section. Table 1 presents our calculated binding and total energies of excitons, obtained using both methods. While the Wannier–Mott model provides reasonable estimates, it slightly underestimates the exciton binding energies compared to BSE calculations. This behavior is consistent with previous studies[27]. The discrepancy arises from two main approximations in the Wannier–Mott model: (i) the effective-mass approximation, which neglects band non-parabolicity and band mixing near the K point; and (ii) the neglect of the electron-hole exchange interaction[27,28]. Overall, there is a good agreement between the model results and those obtained from BSE calculations.
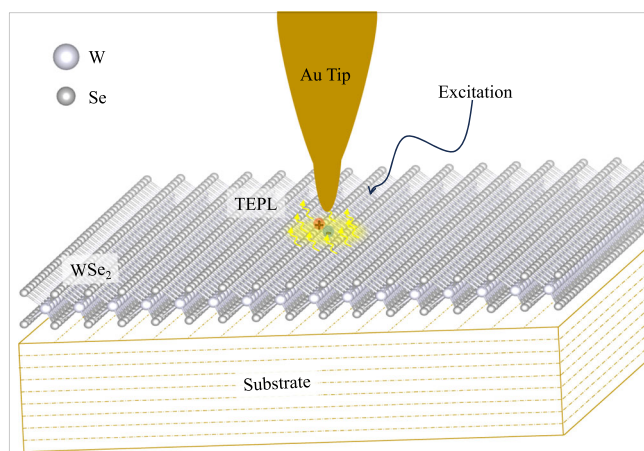
Fig. 1 | Schematic of the Tip-Enhanced Photoluminescence (TEPL) System. This diagram depicts the TEPL setup, where a sharp metallic or plasmonic tip is used to enhance the local electromagnetic field at the sample surface. A tightly focused laser excites the sample, and the near-field interaction between the tip and the material amplifies the photoluminescence signal, enabling high spatial resolution and sensitivity.
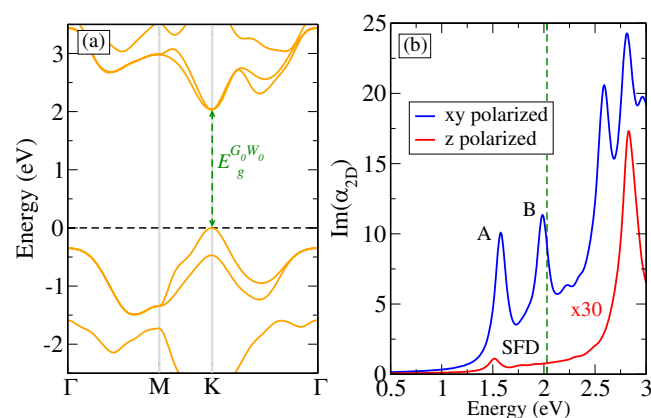
Fig. 2 | Quasiparticle bandstructure and excitonic absorption spectrum of WSe$_2$ ML. a Electronic bandstructure of WSe$_2$ ML calculated using the G_0W_0 approximations. $E_g^{G_0W_0}$ denotes the quasiparticle bandgap. **b** BSE absorption spectrum of WSe$_2$ ML computed with the in-plane polarization (blue) or z-polarization (red). The A and B peaks correspond to optically active (bright) excitons. The SFD label marks the spin-forbidden dark exciton. The vertical green line indicates the G_0W_0 electronic gap.

Furthermore, the dielectric environment of the WSe$_2$ ML is accounted for via the Rytova-Keldysh potential within the Wannier–Mott model. Specifically, the surrounding medium is described by an effective dielectric constant $\epsilon_m = (\epsilon_{\infty,\text{sub}} + \epsilon_{\infty,\text{tip}})/2$[29], where $\epsilon_{\infty,\text{sub}}$ and $\epsilon_{\infty,\text{tip}}$ are the static dielectric constants of the substrate and the tip, respectively. Given that the tip-monolayer separation exceeds 1 nm, we assume that the top dielectric environment is effectively vacuum ($\epsilon_{\infty,\text{tip}} \simeq 1$). We then explore the influence of the substrate dielectric constant $\epsilon_{\infty,\text{sub}}$ on the binding energy of the $\tilde{1}s$ spin-forbidden dark (SFD) exciton. This approximation is particularly valid for the $\tilde{1}s$ exciton, which is less affected by distant screening and more sensitive to immediate dielectric surroundings[30]. Experimental observations by Kyoung-Duck Park et al.[11] support this assumption, showing that the $\tilde{1}s$ exciton energy remains essentially constant when the tip-ML distance varies from 1 to 12 nm. To reveal the dielectric environment effect, we consider SiO$_2$ and hBN dielectric substrates which are widely used for TMDs[31] (see Table 1). For SiO$_2$ substrate, the SFD exciton binding energy decreases from 440 meV in the freestanding ML to 334 meV due to screening effects. Due to its high dielectric constant ($\epsilon_{\infty,sub} = 3.88$), the hBN substrate results in the lowest exciton binding energy and the highest total energy compared to the SiO$_2$ substrate.
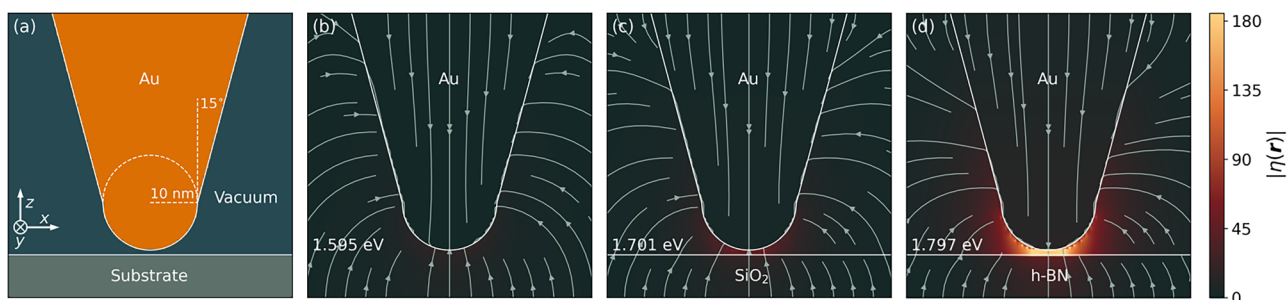
Electric field enhancement around Au tip
Before calculating the excitonic responses of the WSe$_2$ ML, let us discuss the enhancement of the electric field $\mathbf{E}(\mathbf{r})$ around the Au tip that is irradiated by an incident light. Figure 3a depicts the Au tip in the xz plane, with a radius of 10 nm. The tip is rotationally symmetric in the xy plane. Hereafter, we define $z = 0$ as the interface between the substrate and vacuum, as indicated by the horizontal solid line. The electric field $\mathbf{E}_m$ of the incident light is polarized along the z direction. The photon excitation energy corresponds to the dark exciton energy $E_{\tilde{1}s}$ in the Wannier–Mott model, which varies depending on the substrate, as listed in Table 1. In the calculation, the permittivity of Au tip as a function of photon frequency $\varepsilon_{\text{Au}}(\omega)$ is adopted from Vial et al.[32] (see Method). On the other hand, we adopt $\varepsilon_{\text{sub},\infty}$ for the dielectric substrate (corresponding to the high-frequency optical dielectric constant) because the $\varepsilon_{\text{sub}}(\omega)$ is close or equal to $\varepsilon_{\text{sub},\infty}$. The electric field enhancement factor is defined by $|\eta(\mathbf{r})| = |\mathbf{E}(\mathbf{r})/\mathbf{E}_m|$.

Table 1 | Effect of dielectric environment on the binding energy ($e_{\tilde{1}s}^b$) and total energy ($E_{\tilde{1}s}$) of the $\tilde{1}s$ SFD exciton

		BSE		Wannier–Mott model	
	$\epsilon_{\text{sub},\infty}$	$e_{\tilde{1}s}^b$ (meV)	$E_{\tilde{1}s}$ (eV)	$e_{\tilde{1}s}^b$ (meV)	$E_{\tilde{1}s}$ (eV)
Vacuum	1	518	1.52	440	1.595
SiO$_2$	2.16[24]	–	–	334	1.701
h-BN	3.88[24,65]	–	–	236	1.797

The quantity $\epsilon_{\infty,sub}$ denotes the high-frequency dielectric constant of the substrate. For the vacuum case, results from both the BSE and Wannier–Mott models are presented for comparison.

Figure 3b shows $|\eta(\mathbf{r})|$ without substrate. Figure 3b, c, respectively, depicts $|\eta(\mathbf{r})|$ in the presence of the SiO$_2$ and h-BN substrates, which are positioned 1 nm below the tip along the z-axis. Unless otherwise stated, we refer to the region between the lower end of the tip and the substrate as the "nanogap". Figure 3d exhibits the largest $|\eta(\mathbf{r})|$, which is attributed to the large difference between the permittivities of h-BN and vacuum. We can see that $|\eta(\mathbf{r})|$ is localized around nanogap and decays rapidly with increasing distance along the x direction. This phenomenon indicates the near-field enhancement.
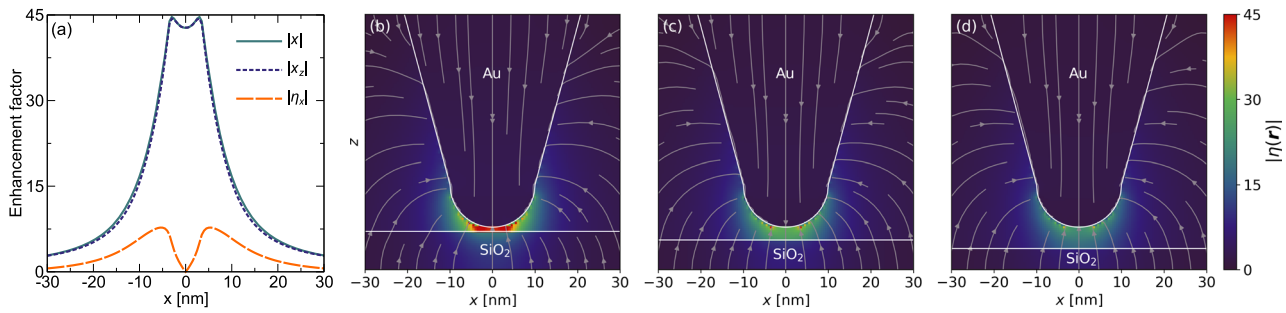
Figure 4a shows $|\eta|$ as a function of x at $z = 0$, which corresponds to the horizontal line in Fig. 4b. The enhancement factors for the electric fields in the x- and z-directions, $|\eta_x|$ and $|\eta_z|$ respectively, are also shown. It can be seen that $|\eta| \approx |\eta_z|$, because within the nanogap, the near-field field is predominantly polarized along the z-direction. In Fig. 4c, d, $|\eta(\mathbf{r})|$ becomes weaker with increasing the size of the nanogap.

Dark exciton activation: selection rules and momentum mismatch
The absorption spectra in Fig. 2 show that z-polarized light activates the SFD exciton. This can be explained by dipole selection rules, specifically through the dipole matrix element $\hat{r}_{cv}$. According to group theory analysis[3,7], the ground state exciton transform according to the representations $\Gamma_X = \Gamma_c \otimes \Gamma_v^*$, where Γ_c corresponds to the representation of the conduction band state and Γ_v represents the representation of the empty valence band state. The dark exciton state belongs to Γ_4 associated with z-polarized light. This excitonic state belongs to the product of the C_{3h} irreducible representations $\Gamma_9 \otimes \Gamma_7^*$, where Γ_9 and Γ_7 correspond to the conduction and valence bands of opposite spin, respectively. As depicted in Fig. 5, these representations illustrate the spin-orbit-induced splitting of electronic states, revealing the symmetry constraints that dictate optical selection rules in WSe$_2$ ML.

In the basis set $\{u_{+1,+1/2}^{8,v}, u_{+1,-1/2}^{7,v}, u_{+1,+1/2}^{9,c}, u_{+1,-1/2}^{12,c}\}$, the only nonzero interband transitions are listed in Table 2. This basis set used in the analysis is directly connected to the lattice-periodic functions $u_{n,\mathbf{k}}(\mathbf{r})$ in Eq. (6). Each basis function $u_{+1,s}^{\Gamma_n,n}(\mathbf{r})$ carries the symmetry and spin-orbit character of the bands at the K point, enabling a group-theoretical analysis of optical transitions. The ratio of the dipole matrix element for the dark exciton (z-polarization) to that of the A bright exciton (in-plane x-polarization) is 3.5×10^{-2}. Since the oscillator strength is proportional to the square of the dipole matrix element, the dark exciton's contribution is reduced by a factor of 10^{-3} compared to that of the bright exciton. This result is in good agreement with previous calculations[1,7]. The weak dipole matrix element for the dark exciton arises from the fact that the involved bands have predominantly opposite effective spin. However, due to spin-orbit spin mixing, a minority spin component in the bands ensures spin conservation for the dark exciton transition[7].

To gain deeper insight into this effect, we project the Kohn–Sham wavefunctions at the K point of the valence and conduction bands onto

Fig. 3 | Near-field enhancement induced by an Au tip with different substrate environments. a The Au tip in the xz plane. Plots $|\eta(\mathbf{r})|$ (color scale) in the xy plane are shown for **b** without a substrate, **c** with a SiO$_2$ substrate, and **d** with a h-BN substrate. The maximum enhancement factors max($|\eta(\mathbf{r})|$) in (**b**), (**c**), and (**d**) are 13.98, 43.79, and 180.42, respectively. The arrows show the directions of $\mathbf{E}(\mathbf{r})$.

Fig. 4 | Dependence of near-field enhancement on nanogap size at the Au tip–SiO$_2$ interface. a $|\eta|$, $|\eta_z|$, and $|\eta_z|$ as a function of x at $z = 0$, corresponding to the surface of the SiO$_2$ substrate in (**b**), as indicated by the horizontal solid line. Plots of $|\eta(\mathbf{r})|$ (color scale) in the xz-plane for nanogap sizes of **b** 1 nm, **c** 3 nm, and **d** 5 nm.

The maximum enhancement factors max($|\eta(\mathbf{r})|$) in (**b**), (**c**), and (**d**) are 43.79, 28.86, and 22.91, respectively. The arrows show the directions of $\mathbf{E}(\mathbf{r})$. The position $z = 0$ denotes the topmost surface of the substrate, marked by a solid horizontal line.
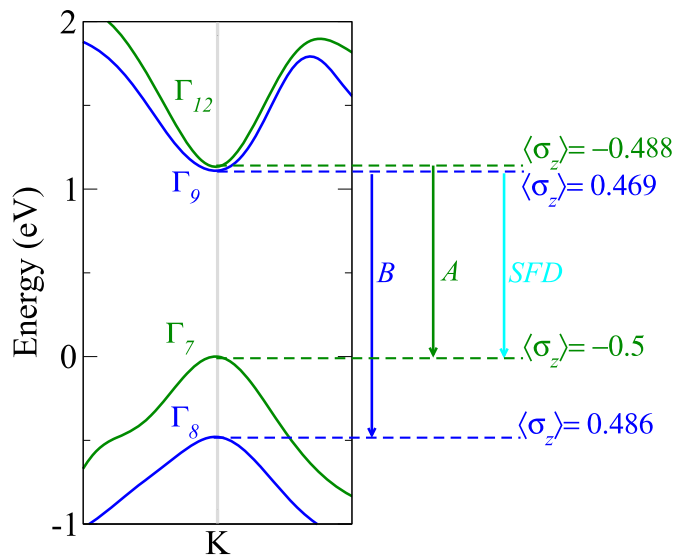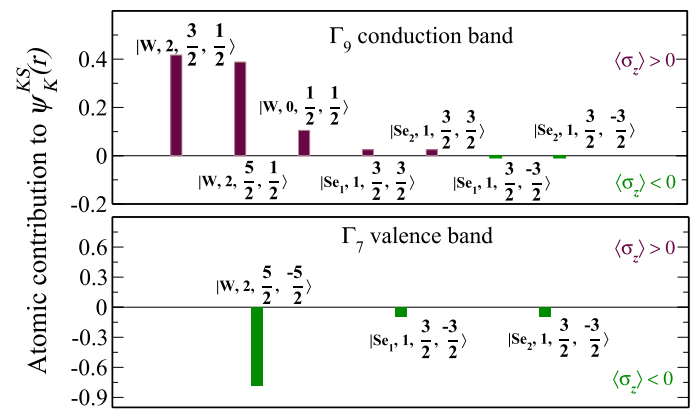

Fig. 5 | Symmetry assignment of the spin-orbit split conduction and valence bands at the K point. The symbols Γ_i denotes the irreducible representations of C_{3h} at K point. $\langle\sigma_z\rangle$ represents the effective spin of each band. The excitonic states A and B correspond to the bright excions, while SFD represents the dark exciton.

Fig. 6 | Projected KS wavefunctions $\Psi_K^{KS}(\mathbf{r})$ in Eq. (6) of the Γ_7 valence band (lower panel) and Γ_9 conduction band (upper panel) onto atomic orbitals within the spin-orbit coupling basis set $\{|atom, l, j, m_j\rangle\}$. Here, l represents the orbital angular momentum, j the total angular momentum, and m_j its projection. Positive (negative) $\langle\sigma_z\rangle$ indicates dominant spin-up (spin-down) contributions.

Table 2 | Dipole matrix elements (in units of the hydrogen Bohr radius a_0) for optical transitions between the bands shown in Fig. 5 at the K point for bright excitons A and B, and the dark exciton SFD, under the corresponding polarization

Exciton	Dipole matrix element (a_0)	Polarization direction
SFD	$\left|\langle u_{+1,-1/2}^{7,v}\|z\|u_{+1,+1/2}^{9,c}\rangle\right| = 0.137$	z
A	$\left|\langle u_{+1,-1/2}^{7,v}\|x\|u_{+1,-1/2}^{12,c}\rangle\right| = 3.897$	x (or y)
B	$\left|\langle u_{+1,+1/2}^{8,v}\|x\|u_{+1,+1/2}^{9,c}\rangle\right| = 2.682$	x (or y)

atomic orbitals within the spin-orbit coupling basis set $\{|atom, l, j, m_j\rangle\}$, as shown in Fig. 6. Here, l denotes the orbital angular momentum, j the total angular momentum, and m_j its projection. While the valence band is entirely formed by spin-down states, a minority of spin-down states $|Se_1, 1, \frac{3}{2}, -\frac{3}{2}\rangle$ and $|Se_2, 1, \frac{3}{2}, -\frac{3}{2}\rangle$ contribute to the electronic wavefunction of the conduction states. According to the dipole selection rules, which require $\Delta l = 0, \pm 1$, $\Delta j = 0, \pm 1$, and $\Delta m_j = 0, \pm 1$, these minority spin components facilitate the dark exciton transition. Indeed, this transition originates from the valence band state $|W, 1, \frac{3}{2}, -\frac{3}{2}\rangle$ to conduction band states

$|Se_1, 1, \frac{3}{2}, -\frac{3}{2}\rangle$ and $|Se_2, 1, \frac{3}{2}, -\frac{3}{2}\rangle$, which conserve spin direction. Finally, both the group theory analysis and the projected wavefunctions confirm that the dipole selection rules allow transitions between the two bands of opposite total spin.

In the absence of a tip, the radiative recombination of SFD excitons remains highly suppressed. This suppression arises from strict energy and momentum conservation, which limits the coupling of the exciton out-of-plane dipole to available photon modes. To quantify this effect, we consider the radiative decay rate $\gamma_{\tilde{1}s}(\mathbf{Q})$ of a $\tilde{1}s$ SFD exciton in the absence of the tip,

$$\gamma_{\tilde{1}s}(\mathbf{Q}) = \frac{\pi e^2 E_{\tilde{1}s}^2(\mathbf{Q})|\hat{z}_{cv}|^2}{\epsilon_0 \hbar^2 c^2}|\phi_{\tilde{1}s}(\mathbf{0})|^2 \frac{1}{|\mathbf{k}_m|^2}\frac{Q^2}{\sqrt{|\mathbf{k}_m|^2 - Q^2}}, \quad (1)$$

where $\hat{z}_{cv}$ represents the out-of-plane interband dipole matrix element, and $\phi_{\tilde{1}s}(\mathbf{0})$ is the relative-motion exciton wavefunction evaluated at zero electron-hole separation. The exciton of wavevector $\mathbf{Q}$ is coupled to photons with $\mathbf{k}_m = (\mathbf{k}_{m,\|}, k_{m,z})$, with the same in-plane wavevector but with all possible values of $k_{m,z}$. The total energy of the $\tilde{1}s$ SFD exciton is given by $E_{\tilde{1}s}(\mathbf{Q}) = E_g^{G_0 W_0} + \frac{\hbar^2}{2M}Q^2 + e_{\tilde{1}s}$, where M is the total exciton mass, and $e_{\tilde{1}s}$ is the eigenvalue of the relative-motion exciton Hamiltonian. The binding energy of the exciton is defined as $e_{\tilde{1}s}^b = -e_{\tilde{1}s}$. Eq. (1) was also found for exciton confined in quantum wells[14].

Eq. (1) establishes two conditions required to activate dark exciton states. First, the dark exciton with energy $E_{\tilde{1}s}(Q)$ emits a photon with an
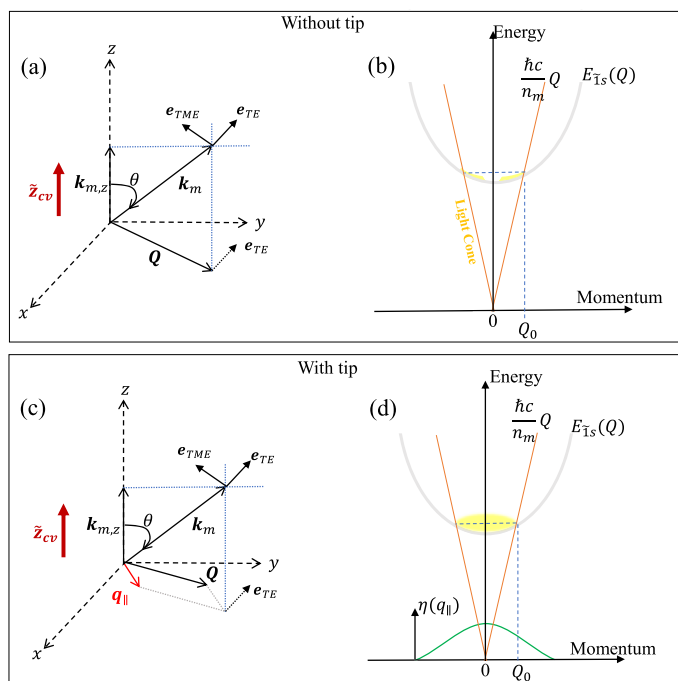
Fig. 7 | **Polarization modes and tip-induced coupling mechanisms for SFD excitons in WSe₂ ML. a–c** Polarization modes and momentum mismatch for dark excitons in 2D TMDs. The diagram illustrates the components of the emitted photon's wavevector, k_m, and highlights two distinct polarization modes: the Transverse Electric (TE) mode, where the electric field lies entirely in-plane, and the Transverse Magnetic-Electric (TME) mode, which includes electric field components in all three directions, allowing interaction with the out-of-plane dipole $\hat{z}_{cv}$ of the SFD exciton. Schematic representation of the $\tilde{1}s$ dark exciton dispersion curve for a WSe₂ ML, and the radiative light cone. Panels (**a**) and (**b**) show the case without a sharp metallic tip, while panels (**c**) and (**d**) depict the scenario with the tip.

out-of-plane momentum $k_{Bz} = \sqrt{k_m^2 - Q^2}$, where $k_m = |\mathbf{k}_m| = n_m E_{\tilde{1}s}(Q)/\hbar c$ is the total wavevector of the emitted photon in the surrounding medium characterized by the effective optical refraction index n_m. This relation imposes the constraint $E_{\tilde{1}s}(Q) \geq \hbar c Q/n_m$ which defines the light cone, as shown in Fig. 7. The photon dispersion, given by $\hbar c Q/n_m$, sets a lower energy threshold for allowed radiative recombination. This condition is also valid for bright excitons[14,33]. Second, a key distinction for dark excitons is that at $\mathbf{Q} = \mathbf{0}$, they remain completely non-radiative due to momentum mismatch.

As established, at $\mathbf{Q} = \mathbf{0}$, dark excitons remain completely non-radiative due to momentum mismatch. This can be further understood by examining the polarization characteristics of the emitted photon, as illustrated in Fig. 7. Since the wavevector $\mathbf{k}_m$ is not strictly parallel to the ML plane, two distinct polarization modes arise. The Transverse Electric (TE) mode, where the electric field lies entirely in the in-plane (x, y) directions, prevents coupling to the out-of-plane dipole $\hat{z}_{cv}$. Conversely, the Transverse Magnetic-Electric (TME) mode contains electric field components in all three directions (x, y, z), allowing interaction with $\hat{z}_{cv}$. However, for $\mathbf{Q} = \mathbf{0}$ (corresponding to $\theta = 0$), the z-component of the TME mode vanishes, eliminating this coupling and further reinforcing the need for a finite in-plane exciton momentum $(\mathbf{Q} \neq \mathbf{0})$ to enable radiative decay.

The presence of a sharp metallic tip modifies the local electromagnetic field, introducing an additional in-plane momentum component. This modification effectively mitigates the momentum mismatch, allowing dark excitons to couple to the out-of-plane optical modes. Using a semiclassical approach for spontaneous emission, the radiative decay rate of dark excitons in the presence of the metallic tip is
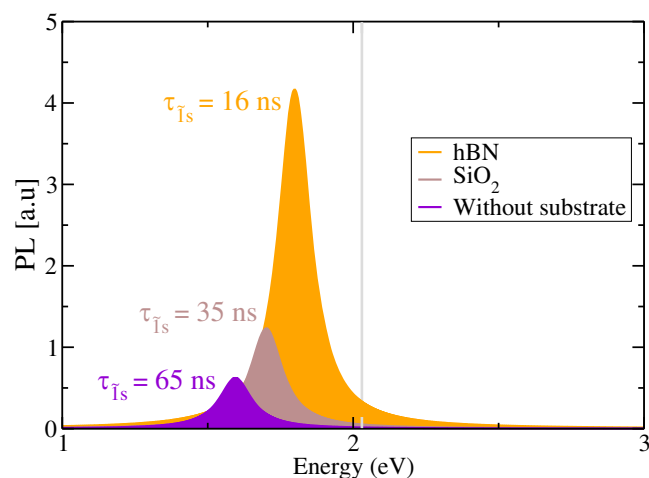
Fig. 8 | **Impact of the substrate on tip-enhanced photoluminescence and radiative life time.** The nanogap distance is fixed to 1 nm.

given by,

$$\gamma_{\tilde{1}s}(\mathbf{Q}) = \pi \frac{e^2 E_{\tilde{1}s}^2(\mathbf{Q})|\hat{z}_{cv}|^2}{\epsilon_0 \hbar^2 c^2} \frac{|\phi_{\tilde{1}s}(\mathbf{0})|^2}{k_m^2}$$
$$\times \int d^2 q_{\parallel} \, \hat{\eta}_z(q_{\parallel}) \frac{|\mathbf{q}_{\parallel} + \mathbf{Q}|^2}{\sqrt{k_m^2 - |\mathbf{q}_{\parallel} + \mathbf{Q}|^2}}, \tag{2}$$

where $\hat{\eta}_z(q_{\parallel}) = \int d^2 \rho \, e^{-i\mathbf{q}\cdot\boldsymbol{\rho}} \eta_z(\rho)$ denotes the two-dimensional Fourier transform of the spatially varying enhancement factor $\eta_z(\rho)$ induced by the metallic tip. (See Eq. (34).) The integral reflects the enhanced recombination probability due to the additional in-plane momentum $q_{\parallel}$. As shown in Fig. 7, this $q_{\parallel}$ compensates for the momentum mismatch, even when $Q = 0$. The z-polarized tip-enhanced electric field generates in-plane momentum, enabling the selective activation of otherwise optically inactive SFD excitons. This process opens new possibilities for controlling and detecting SFD excitons in near-field optical experiments[11].
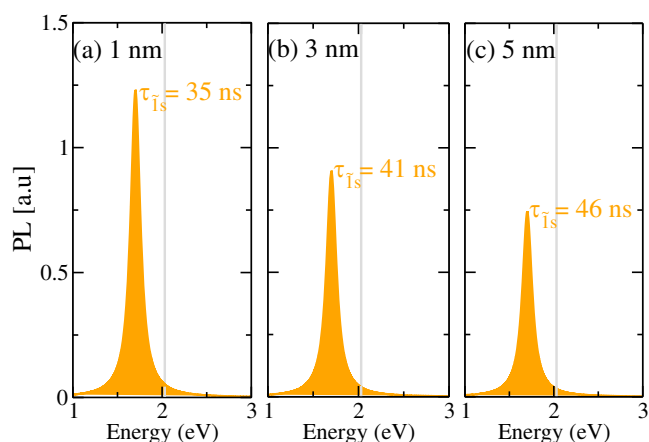
Tip effect on photoluminescence and radiative lifetime of the SFD exciton

To analyze the effect of a sharp metallic tip on the photoluminescence (PL) of the $\tilde{1}s$ SFD exciton, we employ the Elliott formula[34], adapted to a tip-enhanced near-field configuration. The following expression is derived from Eq. (36) introduced in the Microscopic Model (Section 4.5),

$$I_z(\hbar\omega) \propto |\phi_{\tilde{1}s}(0)|^2 |\hat{z}_{cv}|^2 \frac{|\hat{\eta}_z(\mathbf{0})|^2 (\hbar\gamma_{\tilde{1}s}(\mathbf{0}) + \gamma_0)}{(E_{\tilde{1}s}(\mathbf{0}) - \hbar\omega)^2 + (\hbar\gamma_{\tilde{1}s}(\mathbf{0}) + \gamma_0)^2}. \tag{3}$$

Here, $\gamma_{\tilde{1}s}(\mathbf{0})$ is the radiative decay rate of the SFD exciton at zero center-of-mass momentum, while γ_0 accounts for nonradiative broadening, which arises from exciton-phonon interactions and other dephasing mechanisms. The term $|\hat{\eta}_z(\mathbf{0})|^2$ quantifies the local electric field enhancement at the exciton position, which directly influences the PL intensity.

Figure 8 illustrates the PL spectra for different substrate configurations: Au, SiO₂, and without a substrate. The results reveal a significant enhancement in PL intensity when considering substrates compared to the vacuum case. However, despite the stronger local field enhancement in the presence of a gold substrate, the difference in PL intensity between Au and SiO₂ remains relatively small. This is due to competition between both the effect on the relative motion $(\phi_{\tilde{1}s}(0))$ and the enhancement of the electric field $(\hat{\eta}_z(0))$ under different dielectric constants. This suggests a competition

Fig. 9 | Impact of nanogap size on tip-enhanced photoluminescence and radiative lifetime of SFD exciton for a WSe$_2$ monolayer on SiO$_2$ substrate. Panels (**a**), (**b**), and (**c**) correspond to nanogap sizes of 1 nm, 3 nm, and 5 nm, respectively.

between two effects: the enhancement of the local electric field and modifications to the exciton wavefunction due to the dielectric environment.

Additionally, we calculate the radiative lifetime of the SFD exciton at low temperatures (T). In fact, according to ref. 3, for $T < 40$ K, the SFD exciton decay is dominated by radiative recombination. The radiative lifetime, defined as $\tau_{\tilde{1}s} = \gamma_{\tilde{1}s}^{-1}(\mathbf{0})$ of dark excitons, exhibits a strong dependence on the substrate. The calculated values–$\tau_{\tilde{1}s} = 65$ ns in vacuum, $\tau_{\tilde{1}s} = 35$ ns for SiO$_2$ substrate, and $\tau_{\tilde{1}s} =16$ ns for hBN substrate–demonstrate a significant reduction in lifetime due to enhanced radiative recombination. This highlights the critical role of near-field effects in modifying the optical response of dark excitons, paving the way for tunable exciton emission in 2D materials.

Furthermore, Fig. 9 illustrates the impact of the nanogap distance on the PL intensity and radiative lifetime of the $\tilde{1}s$ SFD exciton. As the nanogap size increases, the PL intensity decreases, while the radiative lifetime exhibits an increasing trend. This inverse relationship highlights the role of the nanogap in modifying the local electromagnetic environment, where a smaller gap enhances the exciton's coupling to optical modes, leading to stronger emission and shorter radiative lifetime.

Discussion
The results presented above reveal the essential role of the local electromagnetic environment in activating SFD excitons in WSe$_2$ MLs. A sharp metallic tip enhances both the local field and the in-plane momentum components, thereby overcoming the intrinsic suppression of radiative recombination. Without the tip, the z-polarized dipole matrix element of the SFD exciton is extremely weak due to its origin in spin-mixed conduction band states. Moreover, at zero in-plane momentum ($\mathbf{Q} = \mathbf{0}$), SFD emission is strictly forbidden by momentum conservation. The tip-induced near field not only amplifies the radiative rate but also provides additional in-plane momentum, enabling efficient coupling of SFD excitons to optical modes and promoting radiative decay.

Our findings also highlight the critical influence of the dielectric environment. A higher dielectric constant, as in hBN substrates, screens the Coulomb interaction, resulting in reduced exciton binding energy. At the same time, it enhances the strength of the local electric field near the tip. This combined effect explains the shorter radiative lifetimes observed on hBN compared to vacuum or SiO$_2$ substrates. Furthermore, increasing the nanogap size is found to reduce the PL intensity and increase the radiative lifetime. These results suggest that the radiative lifetime of SFD excitons can be effectively controlled by tuning both the dielectric environment and the tip-ML distance.

Our calculations predict long-lived SFD excitons with radiative lifetimes between 16 and 65 ns, depending on the substrate and tip-ML distance (Figs. 8 and 9). These values are comparable to those reported

for interlayer excitons in WS$_2$/MoSe$_2$ heterobilayers under TEPL[35]. They also agree with a previous estimate of 28 ns for magnetically brightened dark excitons in WSe$_2$ ML[4]. In that study, the measured emission time was 230 ps, limited by nonradiative channels. Robert et al.[3] also reported a decay time of about 110 ps, which sets a lower bound on the radiative lifetime. Our results are consistent with these findings, as they isolate the intrinsic radiative component.

Although the tip modifies the local electromagnetic field, it does not alter the optical selection rules dictated by the crystal symmetry and electronic states. Consequently, Eq. (2) remains valid for the four 2D TMDs namely WS$_2$, WSe$_2$, MoS$_2$, and MoSe$_2$ as they share the same dipole selection rules[7]. However, different TMDs exhibit different SFD exciton energies, which may influence their quantitative response to tip-enhanced radiative decay. Investigating these material-specific effects represents an intriguing avenue for future research.

Methods: microscopic model
The interaction between dark excitons and light in 2D TMD semiconductors is governed by selection rules, excitonic wavefunctions, and the local electromagnetic environment. While SFD excitons possess weak out-of-plane dipole moments, their optical activation remains suppressed due to momentum mismatch with freely propagating photons. In this section, we develop a microscopic framework to describe the tip-induced enhancement of dark exciton emission.

First, we model excitonic states in monolayer WSe$_2$ using two complementary approaches: the BSE, which accounts for many-body interactions, and the Wannier–Mott model, which provides an analytical treatment of excitonic binding energies. We then analyze the local electromagnetic field enhancement near a sharp metallic tip and derive the exciton-photon interaction Hamiltonian in the presence of the tip. Finally, we derive the spontaneous emission rate of dark excitons, demonstrating how the tip facilitate radiative recombination. This microscopic model provides insights into controlling dark exciton emission and radiative lifetime engineering in 2D materials.

Exciton models
To accurately capture excitonic effects, one must solve the Bethe–Salpeter Equation (BSE), which originates from many-body perturbation theory[15,16]. The process begins by determining the single-particle eigenvalues and wavefunctions, which serve as inputs for the BSE. In 2D TMD semiconductors, standard DFT typically underestimates the bandgap[25,36]. To address this, the non-self-consistent G_0W_0 correction is employed[37]. Here, the dielectric function in the screened Coulomb potential (W) and the wavefunctions and energies in the Green's function (G) are not iteratively updated. The DFT + G_0W_0 approach balances computational efficiency and accuracy for TMDs[25,36]. In particular, the electronic structure calculations are carried out within DFT formalism using the Quantum Espresso (QE) code[38,39], while the G_0W_0 bandgap correction is calculated using the YAMBO code[15,16]. By first refining the electronic structure with DFT + G_0W_0 and then solving the BSE, this methodology provides an accurate framework for investigating excitonic effects in WSe$_2$ MLs.

The BSE Hamiltonian is defined in the basis of electron-hole pairs $|vc\mathbf{k}\rangle$. This Hamiltonian includes the single particle energies $\epsilon_{c\mathbf{k}}$ and $\epsilon_{v\mathbf{k}}$, along with an interaction kernel K_{eh}. This latter describes screened Coulomb and exchange interactions. The eigenvalue equation is expressed as[16],

$$(\epsilon_{c\mathbf{k+Q}} - \epsilon_{v\mathbf{k}})A_{vc\mathbf{k}}^{\kappa} + \sum_{\mathbf{k}'v'c'} \langle vc\mathbf{k}|K_{eh}|v'c'\mathbf{k}'\rangle A_{v'c'\mathbf{k}'}^{\kappa} \\ = \hbar\omega_{\kappa} A_{vc\mathbf{k}}^{\kappa}, \tag{4}$$

Here, we label exciton states by $\kappa \equiv (\lambda, \mathbf{Q})$, where λ collects internal quantum numbers (e.g., $\tilde{n}$, s, valley, spin) and $\mathbf{Q}$ is the center-of-mass momentum of the exciton. $\hbar\omega_{\kappa}$ is the energy of the exciton state κ. The exciton

wavefunction is represented as a sum of electron-hole pair states,

$$|\Psi_\kappa^{ex}\rangle = \sum_{v,c,\mathbf{k}} A_{vc\mathbf{k}}^\kappa |v,\mathbf{k}\rangle |c,\mathbf{k}+\mathbf{Q}\rangle, \tag{5}$$

where the coefficients $A_{vc\mathbf{k}}^\kappa$ determine the contribution of each pair state. The single-particle states $\Psi_{n,\mathbf{k}}^{KS}(\mathbf{r}) = \langle r|n,\mathbf{k}\rangle^{KS}$ used in BSE (4) follow Bloch theorem,

$$\Psi_{n,\mathbf{k}}^{KS}(\mathbf{r}) = e^{i\mathbf{k}\cdot\mathbf{r}} u_{n,\mathbf{k}}(\mathbf{r}) = \sum_{\mathbf{g}} C_{\mathbf{k},\mathbf{g}} e^{i(\mathbf{k}+\mathbf{g})\cdot\mathbf{r}}, \tag{6}$$

where $C_{\mathbf{k},\mathbf{g}}$ are the plane-wave expansion coefficients determined during the DFT calculation. $\mathbf{g}$ denotes a reciprocal lattice vector, accounting for the crystal's periodicity in reciprocal space. The periodic part of the Bloch function, $u_{n,\mathbf{k}}(\mathbf{r})$, carries the crystal symmetry information, with n denoting the band index (either conduction or valence). In TMDs, group theory analysis provides valuable information on the symmetry properties of electronic states and their corresponding excitons[3,7]. In this context, it is convenient to label $u_{n,\mathbf{k}}(\mathbf{r})$ by its irreducible representation Γ_n and the spin index, that is, $u_{n,\mathbf{k}}(\mathbf{r}) \equiv u_{\mathbf{k},s}^{\Gamma_n,n}(\mathbf{r})$. This label captures the relevant symmetry and spin-orbit coupling effects that are crucial in determining optical selection rules in monolayer TMDs.

Finally, the optical absorption spectrum associated with vertical excitonic transitions ($\mathbf{Q} = 0$) is determined by the imaginary part of the polarizability function, expressed as[25],

$$\alpha_{2D}(\omega) = \frac{e^2}{A_{uc}} \sum_\lambda \frac{|C_\sigma^\lambda(\mathbf{0})|^2}{\hbar\omega - \hbar\omega_\lambda(\mathbf{0}) + i\gamma}, \tag{7}$$

where A_{uc} denotes the area of the unit cell. The quantity $C_\sigma^\lambda(\mathbf{Q}) \equiv C_\sigma^\kappa = \sum_{cv\mathbf{k}} A_{vc\mathbf{k}}^\kappa \hat{r}_{cv\mathbf{k}}$ represents the light-matter coupling matrix element for the exciton state κ and light polarization direction σ, where $\sigma = x, y, z$. The dipole matrix element $\hat{r}_{cv\mathbf{k}} = \langle v,\mathbf{k}|\mathbf{r}\cdot\hat{\sigma}|c,\mathbf{k}+\mathbf{Q}\rangle$ describe the electronic transitions from valence to conduction bands and encode the directionality of the dipole operator with respect to the polarization vector $\hat{\sigma}$[15]. The parameter γ denotes the numerical broadening used to mimic the experimental linewidth of absorption peaks by effectively incorporating damping processes such as exciton-phonon and impurity scattering[40]. Here, we use $\gamma = 0.068$ eV, consistent with previous BSE studies of WSe$_2$ ML (0.05 eV)[41,42]. While exciton-phonon scattering typically yields room-temperature broadening of 30–40 meV[43–45], our choice provides a realistic comparison with experiment[46] and ensures that the $\tilde{1}s$ A and B excitonic peaks remain clearly resolved.

The BSE (4) describes excitonic interactions by incorporating multiple valence and conduction bands, leading to large matrix dimensions and high computational costs. A common approximation simplifies the problem by considering only one conduction and one valence band that contribute most significantly to exciton formation[27,28]. In 2D TMD semiconductors, this approach is generally valid due to strong spin-orbit splitting and strict selection rules, which restrict the involvement of other bands in low-energy excitonic states. Under this approximation, Eq. (4) simplifies to,

$$(\epsilon_{c\mathbf{k}+\mathbf{Q}} - \epsilon_{v\mathbf{k}})A_{\mathbf{k}}^\kappa + \sum_{\mathbf{k}'} \langle vc\mathbf{k}|K_{eh}|vc\mathbf{k}'\rangle A_{\mathbf{k}'}^\kappa = \hbar\omega_\kappa A_{\mathbf{k}}^\kappa. \tag{8}$$

In this case, the total exciton wave function is giving by,

$$|\Psi_\kappa^{ex}\rangle \approx \sum_{\mathbf{k}} A_{\mathbf{k}}^\kappa |v,\mathbf{k}\rangle |c,\mathbf{k}+\mathbf{Q}\rangle. \tag{9}$$

Furthermore, the electron and hole bands are assumed to be isotropic and parabolic near the $\mathbf{K}$ points (see Fig. 2b). Thus, the effective-mass approximation (EMA) is applied to describe the low-energy excitonic

states in the considered TMDs[19–24]. The exciton wavefunction in real space in 2D is expressed as,

$$\Psi_\kappa^{ex}(\mathbf{r}_e, \mathbf{r}_h) = \sum_{\mathbf{q}} A_{\mathbf{q}}(\mathbf{Q}) e^{i\mathbf{Q}\cdot\mathbf{R}} e^{i\mathbf{q}\cdot\boldsymbol{\rho}} u_{v,\mathbf{k}}(\mathbf{r}_h) u_{c,\mathbf{k}+\mathbf{Q}}(\mathbf{r}_e), \tag{10}$$

where the coordinates $\mathbf{r}_e = (\boldsymbol{\rho}_e, z_e)$ and $\mathbf{r}_h = (\boldsymbol{\rho}_h, z_h)$ represent their respective positions in the 3D space. To describe the motion of the exciton, we define the relative coordinate $\boldsymbol{\rho} = \boldsymbol{\rho}_e - \boldsymbol{\rho}_h$ and the center-of-mass (CM) coordinate $\mathbf{R} = (m_e\boldsymbol{\rho}_e + m_h\boldsymbol{\rho}_h)/(m_e + m_h)$. The corresponding wavevectors are related to the single electron ($\mathbf{k}_e = \mathbf{k} + \mathbf{Q}$) and hole ($\mathbf{k}_h = -\mathbf{k}$) wavevectors via $\mathbf{Q} = \mathbf{k}_e + \mathbf{k}_h$ and $\mathbf{q} = (m_h\mathbf{k}_e - m_e\mathbf{k}_h)/(m_e + m_h)$. For slowly varying Bloch functions around the $\mathbf{K}$ point, the wave function (10) can be expressed as,

$$\Psi_\kappa^{ex}(\mathbf{r}_e, \mathbf{r}_h) \approx \chi_\kappa(\boldsymbol{\rho}_e, \boldsymbol{\rho}_h)\mathcal{U}^X(\mathbf{r}_e, \mathbf{r}_h), \tag{11}$$

where $\chi_\kappa(\boldsymbol{\rho}_e, \boldsymbol{\rho}_h) = \sum_{\mathbf{q}} A_{\mathbf{q}}(\mathbf{Q}) e^{i\mathbf{Q}\cdot\mathbf{R}} e^{i\mathbf{q}\boldsymbol{\rho}}$ is the envelope function, describing electron-hole interactions, quantum confinement, and external perturbations. The Bloch function of the exciton is $\mathcal{U}^X(\mathbf{r}_e, \mathbf{r}_h) = u_v(\mathbf{r}_h)u_c(\mathbf{r}_e)$, which reflects the crystal symmetry. In agreement with the approximated wave function (11), the two-band BSE problem (8) reduces to the envelope Schrödinger equation of Wannier–Mott exciton,

$$\left\{ -\frac{\hbar^2}{2M}\nabla_R^2 - \frac{\hbar^2}{2\mu_X}\nabla_\rho^2 + V_{SC}(|\boldsymbol{\rho}|) \right\} \chi_\kappa(\mathbf{R}, \boldsymbol{\rho})$$
$$= \left(\hbar\omega_\kappa - E_g^{G_0W_0} \right) \chi_\kappa(\mathbf{R}, \boldsymbol{\rho}), \tag{12}$$

where $M = m_e + m_h$ is the total exciton mass, and $\mu_X = m_e m_h/(m_e + m_h)$ is the reduced exciton mass. The quantity $E_g^{G_0W_0}$ represents the quasiparticle bandgap energy of the ML.

In Eq. (12), $V_{SC}(|\boldsymbol{\rho}|)$ represents the screened Coulomb potential. The Coulomb interaction between charge carriers in 2D materials is strongly influenced by the surrounding dielectric environment, where field lines are screened by adjacent materials[20–22,47,48]. In the Bethe–Salpeter framework, long-range screened Coulomb interactions significantly increase computational costs. However, within the Wannier–Mott exciton model, the environmental screening effect is accounted for using the Rytova-Keldysh potential in the long-wavelength limit[17,18,49],

$$V_{SC}(\rho) = -e^2 \int_0^\infty dq \frac{J_0(\rho q)}{\epsilon_m + 2\pi\alpha_{2D}q}, \tag{13}$$

where $J_0(q\rho)$ is the zeroth-order Bessel function and $\rho = |\boldsymbol{\rho}|$. The effective dielectric constant is given by $\epsilon_m = (\epsilon_{\infty,sub} + \epsilon_{\infty,tip})/2$[29], where $\epsilon_{\infty,sub}$ and $\epsilon_{\infty,tip}$ are the dielectric constants of the substrate and the tip, respectively. According to Florian et al.[30], the $\tilde{1}s$ exciton is primarily sensitive to the immediate surrounding environment, especially adjacent materials. Furthermore, Park et al.[11] experimentally observed that the energy of the $\tilde{1}s$ exciton remains essentially unchanged as the nanogap size increases from 1 to 12 nm. Based on this, we approximate $\epsilon_{\infty,tip} \approx 1$, accounting for the vacuum gap between the tip and the ML. Therefore, the effect of the tip enters exclusively through the enhanced local electric field that modifies the radiative decay rate. The parameter α_{2D} represents the polarizability, which is determined from first-principles calculations[49,50] using Eq. (7).

In Eq. (12), the CM and relative motions of the free exciton are separable. Hence, the solutions can be expressed as the product of the relative motion wave function and the CM wave function $\chi_\kappa(\boldsymbol{\rho}, \mathbf{R}) = \psi(\boldsymbol{\rho}) \Phi(\mathbf{R})$. The CM motion's eigenfunctions and eigenvalues are given by $\Phi_{CM}(\mathbf{R}) = \frac{1}{\sqrt{S}} e^{-i\mathbf{Q}\cdot\mathbf{R}}$ and $E_{CM} = \frac{\hbar^2}{2M}\mathbf{Q}^2$, where S is the normalization surface.

For the relative motion, the wave function $\psi_{\tilde{n}l}(\boldsymbol{\rho})$ is expanded in a basis of 2D hydrogen-like functions, given by $\phi_{n,l}(\boldsymbol{\rho}) = N_{n,l}(a_n\rho)^{|l|} L_{n-|l|-1}^{2|l|}(a_n\rho)e^{-\frac{a_n}{2}\rho}e^{il\theta}$[51]. Here, $n = 1, 2, \ldots, k$ denotes the radial quantum number, while $l = 0, \pm 1, \pm 2, \ldots, \pm(n-1)$ represents the azimuthal quantum number of the relative motion. $L_{n-|l|-1}^{2|l|}(a_n\rho)$ are the associated Laguerre

polynomials, where $a_n = \frac{4}{(2n-1)a_B}$. The normalization constant is given by

$$N_{n,l} = \sqrt{\left(\frac{2}{\pi}\right)\left(\frac{2}{(2n-1)a_B}\right)^2 \frac{(n-|l|-1)!}{(n+|l|-1)!(2n-1)}}, \quad (14)$$

where a_B is the 3D effective Bohr radius, defined as $a_B = \epsilon_B \hbar^2/\mu_X e^2$ [51].

As a result of this section, within the Wannier–Mott model, the total exciton wave function is given by,

$$\Psi^{ex}_{\kappa}(\mathbf{r}_e, \mathbf{r}_h) = \frac{1}{S^{3/2}} \sum_q \hat{\psi}_{\tilde{n}l}(\mathbf{q}) e^{i\mathbf{QR}} e^{iq\rho} \mathcal{U}^X(\mathbf{r}_e, \mathbf{r}_h), \quad (15)$$

where we used the inverse Fourier transform of the relative wave function, $\psi_{\tilde{n}l}(\boldsymbol{\rho}) = \frac{1}{S}\sum_q \hat{\psi}_{\tilde{n}l}(\mathbf{q}) e^{iq\rho}$. In addition, the total energy of the exciton is given by,

$$\hbar\omega_\kappa \equiv E_{\tilde{n}l}(\mathbf{Q}) = E_g^{GW} + \frac{\hbar^2}{2M}\mathbf{Q}^2 + e_{\tilde{n}l}, \quad (16)$$

Hereafter, $\kappa \equiv (\tilde{n}l, \mathbf{Q})$. The last term, $e_{\tilde{n}l}$, represents the exciton binding energy. In this study, we restrict ourselves to the exciton ground relative state ($n = 1$, $l = 0$) denoted $\tilde{1}s$.

Tip-enhanced electric field

In this section, we describe the calculation of enhanced electric field in the vicinity of the Au tip, which is placed in a homogeneous medium with relative permittivity ϵ_m. The tip is illuminated by an incident light whose electric field follows a harmonic time-dependence, $\mathbf{E}_m(\mathbf{r}, t) = \mathbf{E}_m(\mathbf{r})e^{-i\omega t}$. The total electric field $\mathbf{E}(\mathbf{r})$ comprises the incident and scattered electric fields, and depends on the relative permittivity $\epsilon(\mathbf{r})$, as follows:

$$\mathbf{E}(\mathbf{r}) = \mathbf{E}_m(\mathbf{r}) + \int d\mathbf{r}' \mathbf{G}(\mathbf{r}, \mathbf{r}') k_0^2 \Delta\epsilon(\mathbf{r}') \mathbf{E}_m(\mathbf{r}'), \quad (17)$$

where $\Delta\epsilon(\mathbf{r}) = \epsilon(\mathbf{r}) - \epsilon_m$ represents the dielectric contrast and $k_0 = \omega/c$ is the free-space wavevector. $\mathbf{G}(\mathbf{r}, \mathbf{r}')$ is Green's tensor of the the complete system which satisfies Dyson's equation [52],

$$\mathbf{G}(\mathbf{r}, \mathbf{r}') = \mathbf{G}_m(\mathbf{r}, \mathbf{r}') + \int d\mathbf{r}'' \mathbf{G}_m(\mathbf{r}, \mathbf{r}'') k_0^2 \Delta\epsilon(\mathbf{r}'') \mathbf{G}(\mathbf{r}'', \mathbf{r}'), \quad (18)$$

where $\mathbf{G}_m(\mathbf{r}, \mathbf{r}')$ is Green's tensor for the homogeneous background medium, expressed as [53,54],

$$\mathbf{G}_m(\mathbf{r}, \mathbf{r}') = \int d\mathbf{k} \left[\mathbf{I} - \frac{\mathbf{k} \otimes \mathbf{k}}{k_m^2}\right] \frac{e^{i\mathbf{k}\cdot(\mathbf{r}-\mathbf{r}')}}{k_m^2 - k^2}. \quad (19)$$

Here, $k_m = \sqrt{\epsilon_m}k_0$ is the wavevector in the background medium, I is the the identity dyad, and $\otimes$ denotes the outer product.

In our calculation, we assume that the size of the Au tip (~50 nm) is considerably smaller than the Rayleigh length of the incident light ($2\pi/k_m$). Therefore, we can use the quasistatic approximation to compute the electric field enhancement around the tip [55]. Here, the electric field of the incident light is treated as spatially constant because the propagation of light around the tip is instantaneous. As a result, the total electric field can be obtained by solving the Laplace equation

$$\nabla \cdot [\epsilon(\mathbf{r}, \omega)\mathbf{E}(\mathbf{r})] = 0. \quad (20)$$

Particularly for the Au tip, the frequency dependence of the complex permittivity $\epsilon_{Au}(\omega)$ is described by a fitting function proposed by Vial et al.[32], which reproduces the experimental transmission spectra of Au reported by Johnson and Christy[56] in the wavelength range of $\lambda = 500$–1000 nm. $\epsilon_{Au}(\omega)$

comprises the Drude and the Lorentz terms as follows[32]:

$$\epsilon_{Au}(\omega) = \epsilon_\infty - \frac{\omega_D^2}{\omega^2 + i\Gamma_D\omega} - \Delta\epsilon \frac{\omega_L^2}{(\omega^2 - \omega_L^2) + i\Gamma_L\omega}, \quad (21)$$

where $\omega_D = 2\pi \times 2113.6$ THz ($\omega_L = 2\pi \times 640.07$ THz) is the plasma (resonant) frequency, $\Gamma_D = 2\pi \times 15.92$ THz ($\Gamma_L = 104.86$ THz) is the damping constant for the Drude (Lorentz) term, and $\Delta\epsilon = 1.09$ is the weight factor. In the limit of high frequency $\omega \rightarrow \infty$, Eq. (21) converges to $\epsilon_\infty = 5.9673$.

In our paper, we only consider the case where $\mathbf{E}_m(\mathbf{r})$ is homogeneous and polarized in the z-direction, $\mathbf{E}_m = E_m\hat{\mathbf{z}}$. Since both $\mathbf{E}_m$ and the tip geometry [schematically depicted in Fig. 3a] exhibits rotational symmetry about the z axis, $\mathbf{E}(\mathbf{r})$ also exhibits rotational symmetry within the within the xy plane. As a result, Eq. (20) reduces to a 2D problem in the xz plane, which is solved using the finite-difference method[57]. The enhancement factor $\eta_\sigma(\mathbf{r})$ of the σ-component of $\mathbf{E}(\mathbf{r})$ is defined by

$$\eta_\sigma(\mathbf{r}) = \frac{\mathbf{E}(\mathbf{r}) \cdot \hat{\sigma}}{E_m}, \quad (22)$$

where $\hat{\sigma} = \hat{\mathbf{x}}, \hat{\mathbf{y}}, \hat{\mathbf{z}}$. It is noted that $\eta_\sigma(\mathbf{r})$ is a complex number. However, since $|\text{Im}(\epsilon_{Au}(\omega))|$ is small compared to $|\text{Re}(\epsilon_{Au}(\omega))|$ for the optical frequencies[32,58], it follows that $|\text{Im}(\eta_\sigma(\mathbf{r}))|$ is small compared to $|\text{Re}(\eta_\sigma(\mathbf{r}))|$. The enhancement factor $|\eta(\mathbf{r})|$ is thus given by

$$|\eta(\mathbf{r})| = \sqrt{|\eta_x(\mathbf{r})|^2 + |\eta_y(\mathbf{r})|^2 + |\eta_z(\mathbf{r})|^2}. \quad (23)$$

Interaction Hamiltonian

We describe the interaction between exciton and photon states using the minimal coupling Hamiltonian in the generalized Coulomb gauge, where the condition $\nabla \cdot [\epsilon_r(\mathbf{r})\mathbf{A}(\mathbf{r}, t)] = 0$ is imposed. Here, $\mathbf{A}(\mathbf{r}, t)$ represents the vector potential. The interaction Hamiltonian takes the form[59,60],

$$\hat{H}_{int} = \frac{ie}{\hbar}\hat{\mathbf{A}}(\mathbf{r}, t) \cdot [\hat{\mathbf{r}}, \hat{H}_{ex}]. \quad (24)$$

The quantized vector potential is expressed as[59],

$$\hat{\mathbf{A}}(\mathbf{r}, t) = \sum_\mu \sqrt{\frac{\hbar}{2\epsilon_0\omega_\mu}}\left\{\mathbf{A}_\mu(\mathbf{r})a_\mu e^{-i\omega_\mu t} + \mathbf{A}_\mu^*(\mathbf{r})a_\mu^\dagger e^{i\omega_\mu t}\right\}, \quad (25)$$

where the index $\mu = (\mathbf{k}, \sigma)$ represents the combination of the wave vector k and polarization σ. The operators a_μ and $a_\mu^\dagger$ correspond to the annihilation and creation operators of a photon in mode μ, respectively. The quantity ω_μ represents the angular frequency of the photon mode μ. In the far-field regime (without a tip), the field distribution is a plane wave, given by $\mathbf{A}_\mu(\mathbf{r}) = \frac{e^{i\mathbf{k}_m\cdot\mathbf{r}}}{\sqrt{\epsilon_r V}}\mathbf{e}_\mu$ [20,59]. However, the presence of the tip locally modifies the field distribution $\mathbf{A}_\mu(\mathbf{r})$, leading to enhanced and spatially confined electromagnetic interactions.

To construct the exciton-photon interaction Hamiltonian, we express the exciton states using second quantization operators. To this end, we assume that excitons behave as noninteracting bosons due to the low excitation density[34,60]. Consequently, the second-quantized Hamiltonian for the bare exciton field is given by[60],

$$\hat{H}_{ex} = \hbar \sum_\kappa \omega_\kappa b_\kappa^\dagger b_\kappa. \quad (26)$$

Here, $b_\kappa^\dagger = |\kappa\rangle\langle G|$ is the exciton creation operator for the state $|\kappa\rangle$, and $|G\rangle$ represents the ground state of the crystal. Finally, the second-quantized
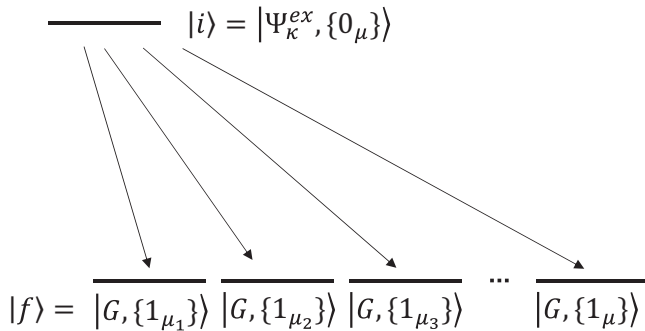
Fig. 10 | Transition from an initial state $|\Psi_\kappa^{ex}, 0_\mu\rangle$ to a set of final states $|G, 1_\mu\rangle$. The states are products of the excitonic state $|\Psi_\kappa^{ex}\rangle$ or the ground state $|G\rangle$ and single-photon states ($|0_\mu\rangle$ or $|1_\mu\rangle$) of a given mode μ.

interaction Hamiltonian can be written as,

$$\hat{H}_{int}^\mu = iC_\mu^{\kappa\dagger}\left(a_\mu^\dagger b_\kappa + a_\mu b_\kappa\right) - iC_\mu^\kappa\left(a_\mu b_\kappa^\dagger + a_\mu^\dagger b_\kappa^\dagger\right), \quad (27)$$

where $C_\mu^\kappa = \hbar\omega_\kappa\left(\frac{e^2}{2\hbar\epsilon_0\omega_\mu}\right)^{1/2}\langle\Psi_\kappa^{ex}|\mathbf{A}_\mu(\mathbf{r})\cdot\hat{\mathbf{r}}|G\rangle$ is the coupling matrix element between the exciton and photon states at a given μ. To evaluate this element, we assume that $A_\mu(\mathbf{r})$ varies slowly over the length scale of the lattice constant[59]. Additionally, we consider that the Bloch functions, which describe the periodic part of the electronic wavefunction, depend only weakly on $\mathbf{k}$ wavevector[59]. Therefore, the coupling matrix element can be written,

$$C_\mu^\kappa = \hbar\omega_\kappa\sqrt{\frac{e^2}{2\hbar\epsilon_0\omega_\mu}}\hat{r}_{cv}\mathbf{e}_\mu\cdot\mathbf{e}_{(r_{cv})}\int d^3r\,\Phi_{CM}(\mathbf{r})A_\mu(\mathbf{r}), \quad (28)$$

where $\mathbf{e}_{(r_{cv})}$ represents the direction of the dipole matrix element, with $\hat{\mathbf{r}}_{cv} = \hat{r}_{cv}\mathbf{e}_{(r_{cv})}$. The vector $\mathbf{e}_\mu$ is a unit vector characterizing the polarization of the optical mode μ.

Spontaneous emission rate

Having established the key elements of our model, we now focus on calculating the spontaneous emission rate of dark excitons. Spontaneous decay is fundamentally a quantum process, best described within the framework of Quantum Electrodynamics (QED). However, due to the unknown electric field distribution near the tip, a semi-classical approach is more suitable. In this case, we employ a method based on the dyadic Green's function[59,61], which accounts for the influence of the electromagnetic environment on the exciton's radiative properties.

We consider the transitions between the states presented in Fig. 10. The initial state $|\Psi_\kappa^{ex}, 0_\mu\rangle$, comprises the exciton with no photons present, while the final state $|G, 1_\mu\rangle$ consists of the system's ground state accompanied by the emission of one photon (see Fig. 10). According to Fermi's golden rule, the radiative decay rate is given by,

$$\gamma_\kappa = \frac{2\pi}{\hbar^2}\sum_\mu\langle G, 1_\mu|\hat{H}_{int}|\Psi_\kappa^{ex}, 0_\mu\rangle$$
$$\times\langle\Psi_\kappa^{ex}, 0_\mu|\hat{H}_{int}|G, 1_\mu\rangle\delta(\omega_\kappa - \omega_\mu), \quad (29)$$

In the following, κ is restricted to the ground relative motion state $\tilde{1}s$ for arbitrary CM momentum $\mathbf{Q}$. Applying the interaction Hamiltonian to both

the initial and final states, the radiative decay rate can be written as,

$$\gamma_{\tilde{1}s}(\mathbf{Q}) = \frac{\pi e^2\omega_{\tilde{1}s}(\mathbf{Q})|\hat{r}_{cv}|^2}{\varepsilon_0\hbar}|\phi_{\tilde{1}s}(0)|^2$$
$$\times\int d^3r\,\Phi_{CM}(\mathbf{r})\int d^3r'\,\Phi_{CM}^*(\mathbf{r}')$$
$$\times\sum_\mu\left[\mathbf{e}_{(r_{cv})}^\dagger\cdot(A_\mu(\mathbf{r})\mathbf{e}_\mu\otimes\mathbf{e}_\mu^\dagger A_\mu^*(\mathbf{r}'))\cdot\mathbf{e}_{(r_{cv})}\right]\delta(\omega_{\tilde{1}s}(\mathbf{Q}) - \omega_\mu). \quad (30)$$

The final term accounts for the contribution from the quantized electromagnetic field, emphasizing the necessity of summing over all possible photon frequencies. To incorporate a classical electric field into this framework, we replace this term with the Green's function, which characterizes the electromagnetic response in the presence of the tip. This substitution allows for a bridge between the quantum mechanical formalism and a semi-classical treatment[61]. The relation between the Green's function tensor and the vector potential is given by[59,61],

$$\text{Im}\left[\mathbf{G}(\mathbf{r}, \mathbf{r}', \omega_{\tilde{1}s}(\mathbf{Q}))\right]$$
$$= \frac{\pi c^2}{2\omega_{\tilde{1}s}(\mathbf{Q})}\sum_\mu\left[A_\mu(\mathbf{r})\mathbf{e}_\mu\right]\otimes\left[\mathbf{e}_\mu^\dagger A_\mu^*(\mathbf{r}')\right]\delta(\omega_{\tilde{1}s}(\mathbf{Q}) - \omega_\mu). \quad (31)$$

Thus, the radiative decay rate can be expressed as,

$$\gamma_{\tilde{1}s}(\mathbf{Q}) = \frac{2e^2\omega_{\tilde{1}s}^2(\mathbf{Q})}{\epsilon_0\hbar c^2}|\hat{r}_{cv}|^2|\phi_{\tilde{1}s}(0)|^2$$
$$\times\int d^3r\,\Phi_{CM}(\mathbf{r})\int d^3r'\,\Phi_{CM}^*(\mathbf{r}')$$
$$\times\{\mathbf{e}_{r_{cv}}^\dagger\cdot\text{Im}\left[\mathbf{G}(\mathbf{r}, \mathbf{r}', \omega_{\tilde{1}s}(\mathbf{Q}))\right]\cdot\mathbf{e}_{r_{cv}}\}. \quad (32)$$

In this study, we focus on the SFD exciton. Since the tip does not alter the dipole selection rules, the dipole matrix element $\hat{r}_{cv}$ adheres to the group theory analysis presented in refs. 3,7. Specifically, these selection rules indicate that the SFD exciton couples to z-polarized light[3]. The dipole matrix element $\hat{z}_{cv}$ corresponds to the transition amplitude between the lowest conduction band and the highest valence band at the $\mathbf{K}$ point[3].

Considering the relationship between the electric field and the Green's function for z-polarized light at the ML located on the substrate surface ($z = 0$), we obtain

$$G_{zz}(\mathbf{r}, \mathbf{r}', \omega_\kappa) = \eta_z(\rho, z = 0)G_{B,zz}(\mathbf{r}, \mathbf{r}', \omega_\kappa). \quad (33)$$

Here, we neglect the imaginary part of the enhancement factor, i.e., $\eta_z(\rho, z = 0) \approx \text{Re}[\eta_z(\rho, z = 0)]$. Using the Fourier transform of $\mathbf{G}(\mathbf{r}, \mathbf{r}', \omega_\kappa)$ presented in (19), Eq. (32) becomes,

$$\gamma_{\tilde{1}s}(\mathbf{Q}) = \pi\frac{e^2\omega_{\tilde{1}s}^2(\mathbf{Q})|\hat{z}_{cv}|^2}{\epsilon_0\hbar c^2}\frac{|\phi_{\tilde{1}s}(0)|^2}{k_m^2}$$
$$\times\int d^2q_\parallel\,\hat{\eta}(q_\parallel)\frac{|\mathbf{q}_\parallel + \mathbf{Q}|^2}{\sqrt{k_m^2 - |\mathbf{q}_\parallel + \mathbf{Q}|^2}}, \quad (34)$$

where $q_\parallel$ represents the momentum transfer induced by the presence of the tip. In the case without the tip, we obtain,

$$\gamma_{\tilde{1}s}(\mathbf{Q}) = \pi\frac{e^2\omega_{\tilde{1}s}^2(\mathbf{Q})}{\epsilon_0\hbar c^2}|\hat{z}_{cv}|^2|\phi_{\tilde{1}s}(0)|^2\frac{1}{k_m^2}\frac{Q^2}{\sqrt{k_m^2 - Q^2}}. \quad (35)$$

Tip-enhanced photoluminescence

The effect of the tip on the SFD exciton can be probed via PL spectroscopy. We consider the weak excitation regime, in which exciton-exciton and exciton-charge interactions are negligible. Assuming a quasi-equilibrium

distribution of excitons, the PL intensity is given by[34,62],

$$I_\sigma(\hbar\omega) = \frac{2}{\hbar} \text{Im} \left[\sum_\kappa \frac{|C_\mu^\kappa|^2}{E_\kappa - \hbar\omega + i(\hbar\gamma_\kappa + \gamma_0)} N_\kappa \right]. \qquad (36)$$

where $N_\kappa = \langle b_\kappa^+ b_\kappa \rangle$ denotes the occupation of the corresponding excitonic state[34]. At low carrier densities, this occupation follows a Boltzmann distribution, $N_\kappa \propto \exp(-\frac{\hbar^2 Q^2}{2Mk_BT})$ where c is a constant[63]. The Eqs. for emission (7) and absorption (36) follow the Elliot formula for exciton[34,62]. Despite their structural similarity, they are distinguished by the presence of the exciton occupation factor, which appears only in the equation of PL[62,64]. Furthermore, the effect of the tip is captured by the matrix element C_μ^κ given by Eq. (28) end the radiative decay rate γ_κ as defined in Eq. (34).

Data availability
The data presented in this study were generated using the mathematical models and computational methods described in the main text and Supplementary Information. All relevant processed data supporting the findings are available from the corresponding author upon reasonable request.

References
1. Echeverry, J., Urbaszek, B., Amand, T., Marie, X. & Gerber, I. C. Splitting between bright and dark excitons in transition metal dichalcogenide monolayers. *Phys. Rev. B* **93**, 121107 (2016).
2. Wang, G. et al. Colloquium: excitons in atomically thin transition metal dichalcogenides. *Rev. Mod. Phys.* **90**, 021001 (2018).
3. Robert, C. et al. Fine structure and lifetime of dark excitons in transition metal dichalcogenide monolayers. *Phys. Rev. B* **96**, 155423 (2017).
4. Zhang, X.-X. et al. Magnetic brightening and control of dark excitons in monolayer WSe₂. *Nat. Nanotechnol.* **12**, 883–888 (2017).
5. Poem, E. et al. Accessing the dark exciton with light. *Nat. Phys.* **6**, 993–997 (2010).
6. Combescot, M., Betbeder-Matibet, O. & Combescot, R. Bose-Einstein condensation in semiconductors: the key role of dark excitons. *Phys. Rev. Lett.* **99**, 176403 (2007).
7. Wang, G. et al. In-plane propagation of light in transition metal dichalcogenide monolayers: optical selection rules. *Phys. Rev. Lett.* **119**, 047401 (2017).
8. Kormányos, A. et al. k.p theory for two-dimensional transition metal dichalcogenide semiconductors. *2D Mater.* **2**, 022001 (2015).
9. Kośmider, K., González, J. W. & Fernández-Rossier, J. Large spin splitting in the conduction band of transition metal dichalcogenide monolayers. *Phys. Rev. B* **88**, 245436 (2013).
10. Molas, M. R. et al. Brightening of dark excitons in monolayers of semiconducting transition metal dichalcogenides. *2D Mater.* **4**, 021003 (2017).
11. Park, K.-D., Jiang, T., Clark, G., Xu, X. & Raschke, M. B. Radiative control of dark excitons at room temperature by nano-optical antenna-tip Purcell effect. *Nat. Nanotechnol.* **13**, 59–64 (2018).
12. Zhou, Y. et al. Probing dark excitons in atomically thin semiconductors via near-field coupling to surface plasmon polaritons. *Nat. Nanotechnol.* **12**, 856–860 (2017).
13. Zhang, X.-X., You, Y., Zhao, S. Y. F. & Heinz, T. F. Experimental evidence for dark excitons in monolayer WSe₂. *Phys. Rev. Lett.* **115**, 257403 (2015).
14. Andreani, L. C., Panzarini, G. & Gérard, J.-M. Strong-coupling regime for quantum boxes in pillar microcavities: theory. *Phys. Rev. B* **60**, 13276 (1999).
15. Sangalli, D. et al. Many-body perturbation theory calculations using the Yambo code. *J. Phys. Condens. Matter* **31**, 325902 (2019).
16. Marini, A., Hogan, C., Grüning, M. & Varsano, D. Yambo: an ab initio tool for excited state calculations. *Comput. Phys. Commun.* **180**, 1392–1403 (2009).
17. Keldysh, L. Coulomb interaction in thin semiconductor and semimetal films. *Sov. J. Exp. Theor. Phys. Lett.* **29**, 658 (1979).
18. Rytova, N. S. The screened potential of a point charge in a thin film. *Mosc. Univ. Phys. Bull.* **3**, 18 (1967).
19. Smiri, A., Amand, T. & Jaziri, S. Optical properties of excitons in two-dimensional transition metal dichalcogenide nanobubbles. *J. Chem. Phys.* **154**, 084110 (2021).
20. Ayari, S., Smiri, A., Hichri, A., Jaziri, S. & Amand, T. Radiative lifetime of localized excitons in transition-metal dichalcogenides. *Phys. Rev. B* **98**, 205430 (2018).
21. Hichri, A., Amara, I. B., Ayari, S. & Jaziri, S. Dielectric environment and/or random disorder effects on free, charged and localized excitonic states in monolayer WS₂. *J. Phys. Condens. Matter* **29**, 435305 (2017).
22. Hichri, A., Ben Amara, I., Ayari, S. & Jaziri, S. Exciton center-of-mass localization and dielectric environment effect in monolayer WS₂. *J. Appl. Phys.* **121**, 235702 (2017).
23. Hannachi, H. E. & Jaziri, S. Stark effect and orbital hybridization of moiré interlayer excitons in the MoSe₂/WSe₂ heterobilayer. *Phys. Chem. Chem. Phys.* **26**, 21753–21766 (2024).
24. Van Tuan, D., Yang, M. & Dery, H. Coulomb interaction in monolayer transition-metal dichalcogenides. *Phys. Rev. B* **98**, 125308 (2018).
25. Reho, R., Botello-Méndez, A. R., Sangalli, D., Verstraete, M. J. & Zanolli, Z. Excitonic response in transition metal dichalcogenide heterostructures from first principles: impact of stacking, twisting, and interlayer distance. *Phys. Rev. B* **110**, 035118 (2024).
26. Molina-Sánchez, A., Sangalli, D., Hummer, K., Marini, A. & Wirtz, L. Effect of spin-orbit interaction on the optical spectra of single-layer, double-layer, and bulk MoS₂. *Phys. Rev. B* **88**, 045412 (2013).
27. Berkelbach, T. C., Hybertsen, M. S. & Reichman, D. R. Theory of neutral and charged excitons in monolayer transition metal dichalcogenides. *Phys. Rev. B* **88**, 045318 (2013).
28. Latini, S., Olsen, T. & Thygesen, K. S. Excitons in van der Waals heterostructures: the important role of dielectric screening. *Phys. Rev. B* **92**, 245123 (2015).
29. Glazov, M. M. & Chernikov, A. Breakdown of the static approximation for free carrier screening of excitons in monolayer semiconductors. *Phys. Status Solidi (b)* **255**, 1800216 (2018).
30. Florian, M. et al. The dielectric impact of layer distances on exciton and trion binding energies in van der Waals heterostructures. *Nano Lett.* **18**, 2725–2732 (2018).
31. Adeniran, O. & Liu, Z.-F. Dielectric screening at TMD: hBN interfaces: monolayer-to-bulk transition, local-field effect, and spatial dependence. *Phys. Rev. Mater.* **7**, 054001 (2023).
32. Vial, A., Grimault, A.-S., Macías, D., Barchiesi, D. & De La Chapelle, M. L. Improved analytical fit of gold dispersion: application to the modeling of extinction spectra with a finite-difference time-domain method. *Phys. Rev. B* **71**, 085416 (2005).
33. Gupta, G. & Majumdar, K. Fundamental exciton linewidth broadening in monolayer transition metal dichalcogenides. *Phys. Rev. B* **99**, 085412 (2019).
34. Brem, S. et al. Phonon-assisted photoluminescence from indirect excitons in monolayers of transition-metal dichalcogenides. *Nano Lett.* **20**, 2849–2856 (2020).
35. May, M. A. et al. Nanocavity clock spectroscopy: resolving competing exciton dynamics in WSe₂/MoSe₂ heterobilayers. *Nano Lett.* **21**, 522–528 (2020).
36. Molina-Sanchez, A., Hummer, K. & Wirtz, L. Vibrational and optical properties of MoS₂: from monolayer to bulk. *Surf. Sci. Rep.* **70**, 554–586 (2015).
37. Hedin, L. New method for calculating the one-particle Green's function with application to the electron-gas problem. *Phys. Rev.* **139**, A796–A823 (1965).

38. Giannozzi, P. et al. QUANTUM ESPRESSO: a modular and open-source software project for quantum simulations of materials. *J. Phys. Condens. Matter* **21**, 395502 (2009).

39. Giannozzi, P. et al. Advanced capabilities for materials modelling with Quantum Espresso. *J. Phys. Condens. Matter* **29**, 465901 (2017).

40. Marini, A. Ab initio finite-temperature excitons. *Phys. Rev. Lett.* **101**, 106405 (2008).

41. Ramasubramaniam, A. Large excitonic effects in monolayers of molybdenum and tungsten dichalcogenides. *Phys. Rev. B* **86**, 115409 (2012).

42. Ataei, S. S. & Sadeghi, A. Competitive screening and band gap renormalization in n-type monolayer transition metal dichalcogenides. *Phys. Rev. B* **104**, 155301 (2021).

43. Selig, M. et al. Excitonic linewidth and coherence lifetime in monolayer transition metal dichalcogenides. *Nat. Commun.* **7**, 13279 (2016).

44. Mueller, T. & Malic, E. Exciton physics and device application of two-dimensional transition metal dichalcogenide semiconductors. *npj 2D Mater. Appl.* **2**, 29 (2018).

45. Henriques, J., Mortensen, N. & Peres, N. Analytical description of the 1s exciton linewidth temperature dependence in transition metal dichalcogenides. *Phys. Rev. B* **103**, 235402 (2021).

46. He, K. et al. Tightly bound excitons in monolayer WSe_2. *Phys. Rev. Lett.* **113**, 026803 (2014).

47. Chernikov, A. et al. Exciton binding energy and nonhydrogenic Rydberg series in monolayer WS_2. *Phys. Rev. Lett.* **113**, 076802 (2014).

48. Kylänpää, I. & Komsa, H.-P. Binding energies of exciton complexes in transition metal dichalcogenide monolayers and effect of dielectric environment. *Phys. Rev. B* **92**, 205418 (2015).

49. Cudazzo, P., Tokatly, I. V. & Rubio, A. Dielectric screening in two-dimensional insulators: implications for excitonic and impurity states in graphane. *Phys. Rev. B* **84**, 085406 (2011).

50. Rasmussen, F. A., Schmidt, P. S., Winther, K. T. & Thygesen, K. S. Efficient many-body calculations for two-dimensional materials using exact limits for the screened potential: band gaps of MoS_2, h-BN, and phosphorene. *Phys. Rev. B* **94**, 155406 (2016).

51. Parfitt, D. & Portnoi, M. The two-dimensional hydrogen atom revisited. *J. Math. Phys.* **43**, 4681–4691 (2002).

52. Martin, O. J. & Piller, N. B. Electromagnetic scattering in polarizable backgrounds. *Phys. Rev. E* **58**, 3909 (1998).

53. Castiaux, A., Girard, C., Dereux, A., Martin, O. J. & Vigneron, J.-P. Electrodynamics in complex systems: application to near-field probing of optical microresonators. *Phys. Rev. E* **54**, 5752 (1996).

54. Arnoldus, H. F. Representation of the near-field, middle-field, and far-field electromagnetic Green's functions in reciprocal space. *JOSA B* **18**, 547–555 (2001).

55. Larsson, J. Electromagnetics from a quasistatic perspective. *Am. J. Phys.* **75**, 230–239 (2007).

56. Johnson, P. B. & Christy, R.-W. Optical constants of the noble metals. *Phys. Rev. B* **6**, 4370 (1972).

57. Pratama, F., Ukhtary, M. S. & Saito, R. Non-vertical optical transition in near-field enhanced spectroscopy of graphene. *J. Phys. Condens. Matter* **31**, 265701 (2019).

58. Etchegoin, P. G., Le Ru, E. & Meyer, M. An analytic model for the optical properties of gold. *J. Chem. Phys.* **125**, 164705 (2006).

59. Stobbe, S. et al. Spontaneous emission from large quantum dots in nanostructures: exciton-photon interaction beyond the dipole approximation. *Phys. Rev. B* **86**, 085304 (2012).

60. Gerace, D. & Andreani, L. C. Quantum theory of exciton-photon coupling in photonic crystal slabs with embedded quantum wells. *Phys. Rev. B* **75**, 235325 (2007).

61. Hecht, B. *Principles of Nano-optics* (Cambridge University Press Textbooks, 2012).

62. Koch, S. W. et al. *Semiconductor Quantum Dots*, vol. 2 (World Scientific, 1993).

63. Rosati, R. et al. Interface engineering of charge-transfer excitons in 2D lateral heterostructures. *Nat. Commun.* **14**, 2438 (2023).

64. Thompson, J. J., Gerhard, M., Witte, G. & Malic, E. Optical signatures of Förster-induced energy transfer in organic/TMD heterostructures. *npj 2D Mater. Appl.* **7**, 69 (2023).

65. Laturia, A., Van de Put, M. L. & Vandenberghe, W. G. Dielectric properties of hexagonal boron nitride and transition metal dichalcogenides: from monolayer to bulk. *npj 2D Mater. Appl.* **2**, 6 (2018).

Acknowledgements

Author contributions
A.S. conceived the idea, developed the theoretical model, and performed the calculations. F.R.P. contributed to the computation of the electric field enhancement. A.S., F.R.P., and T.N. jointly analyzed the results. A.S. wrote the manuscript, with all authors contributing to the discussion and preparation of the final version.

Competing interests
The authors declare no competing interests.

Additional information